buildings

MDPI

*Article*

# Mechanical Behavior and Failure Mechanism of Impact-Damaged RC Columns Strengthened with CFRP: A 3D Meso-Scale Numerical Study

**Yonghui Xing [1,2,3], Fengliang Zhang [1], Zhongqi Shi [2,3,*], Qingrui Yue [2,3,4], Yuzhou Liu [2,3] and Xiaoya Li [5]**

[1] School of Intelligent Civil and Ocean Engineering, Harbin Institute of Technology, Shenzhen 518000, China
[2] Shenzhen Technology Institute of Urban Public Safety, Shenzhen 518000, China
[3] National Science and Technology Institute of Urben Safety Development, Shenzhen 518000, China
[4] Research Institute of Urbanization and Urban Safety, School of Civil and Resource Engineering, University of Science and Technology Beijing, Beijing 100083, China
[5] School of Civil Engineering and Transportation, North China University of Water Resources and Electric Power, Zhengzhou 450045, China
* Correspondence: shizq@szsti.org

**Abstract**

Impact-damaged reinforced concrete (RC) columns often experience significant reductions in load-carrying capacity and ductility when subjected to subsequent axial loading. Carbon fiber-reinforced polymer (CFRP) sheets have been widely used to strengthen such damaged columns; however, the underlying strengthening mechanism remains insufficiently understood, largely due to the difficulty of experimentally capturing the evolution of internal damage. To address this issue, a three-dimensional (3D) meso-scale finite element (FE) model has been developed to investigate the mechanical behavior of CFRP-strengthened impact-damaged RC columns. The proposed model captures the evolution of micro-damage within concrete and provides a more realistic representation of impact-induced damage compared with conventional homogeneous models. The model was first validated against available experimental results, showing good agreement in both failure modes and responses. Based on the validated model, three typical strengthening schemes, including the longitudinally applied CFRP, U-shaped CFRP, and fully wrapped CFRP, are systematically examined in terms of failure patterns, load-carrying capacity, stiffness, ductility, and energy dissipation. The results indicate that the fully wrapped CFRP configuration most effectively mitigated damage in the impact-affected zone and increased the load-carrying capacity by up to 86%. Furthermore, a quantitative evaluation framework based on strengthening indices for axial capacity and energy dissipation is proposed, indicating that strengthening with two CFRP layers can lead to a desirable ductile failure mode within the scope of this numerical investigation. These findings provide useful mechanistic insights into the strengthening process and offer preliminary guidance for the rehabilitation of impact-damaged RC columns, though further validation is required before practical implementation.

**Keywords:** impact-damaged columns; CFRP strengthening; CFRP sheet; mechanical performance; meso-scale modeling

Check for updates

Academic Editor: Giuseppina Uva

Received: 9 March 2026
Revised: 17 April 2026
Accepted: 22 April 2026
Published: 25 April 2026

**Copyright:** © 2026 by the authors. Licensee MDPI, Basel, Switzerland. This article is an open access article distributed under the terms and conditions of the Creative Commons Attribution (CC BY) license.

## 1. Introduction

Under impact loads from terrorist attacks, vehicle or vessel collisions, rockfalls, and other hazards, reinforced concrete (RC) columns exhibit dynamic behaviors that are far

more complex than those under static loading. They are prone to inclined cracks, irreversible deformations, and sudden failure of critical elements, leading to unpredictable losses [1,2]. Many existing RC columns are designed with minimal consideration of impact effects, resulting in a growing demand for retrofitting. Strengthening columns is often more time- and cost-effective than demolition and reconstruction.

Early strengthening methods, such as steel plate and reinforced concrete jackets, increased load capacity but suffered from long construction periods and corrosion-related issues [3]. To overcome these limitations, carbon fiber-reinforced polymer (CFRP) was developed at UCSD Powell Labs. Its high tensile strength and corrosion resistance make it effective for enhancing the load-carrying capacity and ductility of concrete columns [4–7]. Partially strengthened columns, however, often show only marginal improvements compared with fully strengthened ones [2,8,9], and strain-rate effects, which are critical under dynamic loading, are often neglected [10–13]. Liu and Li [14] found that CFRP improved ultimate drift and toughness indices in corrosion-damaged RC columns under seismic loading, although its performance is slightly lower than that of PET-600-strengthened columns. Karayannis et al. [15] and Xu et al. [16] confirmed that CFRP effectively enhances the load-carrying capacity, ductility, and stiffness of damaged beam-column joints. Studies on concrete beams indicate that increasing the number of CFRP layers further improves structural capacity [17–20]. Recent studies show that CFRP confinement influences steel–concrete bond behavior and can be effectively evaluated using machine learning and reliability analysis [21,22].

Most of these studies remain qualitative, with limited quantitative analysis of different CFRP strengthening strategies, especially under impact loads. Concrete, composed of aggregates, mortar, and pores, is an inherently heterogeneous material, producing discrete and random cracks. Most finite element (FE) models treat it as homogeneous, thereby obscuring the mechanisms by which CFRP suppresses damage and limiting mechanistic optimization. To address this, a three-dimensional (3D) meso-scale FE model is developed to capture micro-damage evolution and directly link CFRP confinement to both microstructural damage suppression and macroscopic improvements in load-carrying capacity and ductility.

FRP is a promising material for strengthening damaged RC columns, particularly under impact. Laboratory impact testing, especially under vertical loading, is challenging, making FE modeling essential. Previous models have ignored concrete heterogeneity and failed to clarify the damage mechanisms of CFRP-strengthened, impact-damaged columns. In this study, a 3D meso-scale FE model considering concrete heterogeneity and strain-rate effects is established to realistically simulate impact damage mechanisms and is validated against experiments. By resolving concrete at the meso-scale, this model visualizes how CFRP confinement suppresses micro-crack initiation and propagation, providing mechanistic insight unavailable in homogeneous models.

Three strengthening schemes, including longitudinal CFRP, U-shaped CFRP, and fully wrapped CFRP, are investigated, and their effects on failure patterns, load-carrying capacity, stiffness, ductility, and energy dissipation are quantitatively analyzed. This analysis establishes a causal link between CFRP confinement and observed macroscopic performance. Finally, an evaluation framework combining axial capacity and energy dissipation indices is proposed to translate these meso-scale insights into potential engineering guidance. By positioning this study as a mechanistic and comparative numerical investigation, it aims to reveal underlying damage suppression mechanisms and provide theoretical references for future practical design applications.

## 2. Finite Element Simulation Method

Before the investigation of CFRP strengthening methods on the impact behavior of RC columns using FE, the accuracy of the FE models should be verified against experimental data. Due to rare experimental investigation of the CFRP-strengthened damaged column under the combined impact and axial load, the modeling of the impact process and the axial load process should be verified separately using two types of different experiments. Hence, test data from the literature [23–25] were selected to validate the accuracy of the FE model. The selected specimens were subjected only to impact loads without axial compressive loads. Additionally, test data in the literature [26,27] were selected to verify the accuracy of the FE model of the CFRP-strengthened damaged column under axial loads.

### *2.1. Geometric Model*

Figure 1a displays the specimen details of RC columns obtained from the literature [23]. The size and configuration of the FE model were the same as those of the experimental column. The column had a 150 mm × 150 mm cross-section and a height of 2500 mm, with a distance of 1800 mm between two supports. Longitudinal reinforcement bars with a diameter of 12 mm were arranged at each corner of the cross-section. Stirrups with a diameter of 8 mm and a spacing of 75 mm were arranged within a distance of 350 mm from each end of the column, while the spacing of stirrups was 150 mm in the remaining region. The hinge support at both ends of the column was used in the test. Figure 1b presents the setup of the impact experiments, with the column placed horizontally on the device. An axial compression of 145 kN was applied on the column end. A drop weight with a mass of 215 kg was used to apply the impact load to the column, and its initial velocity was 5.42 m/s.

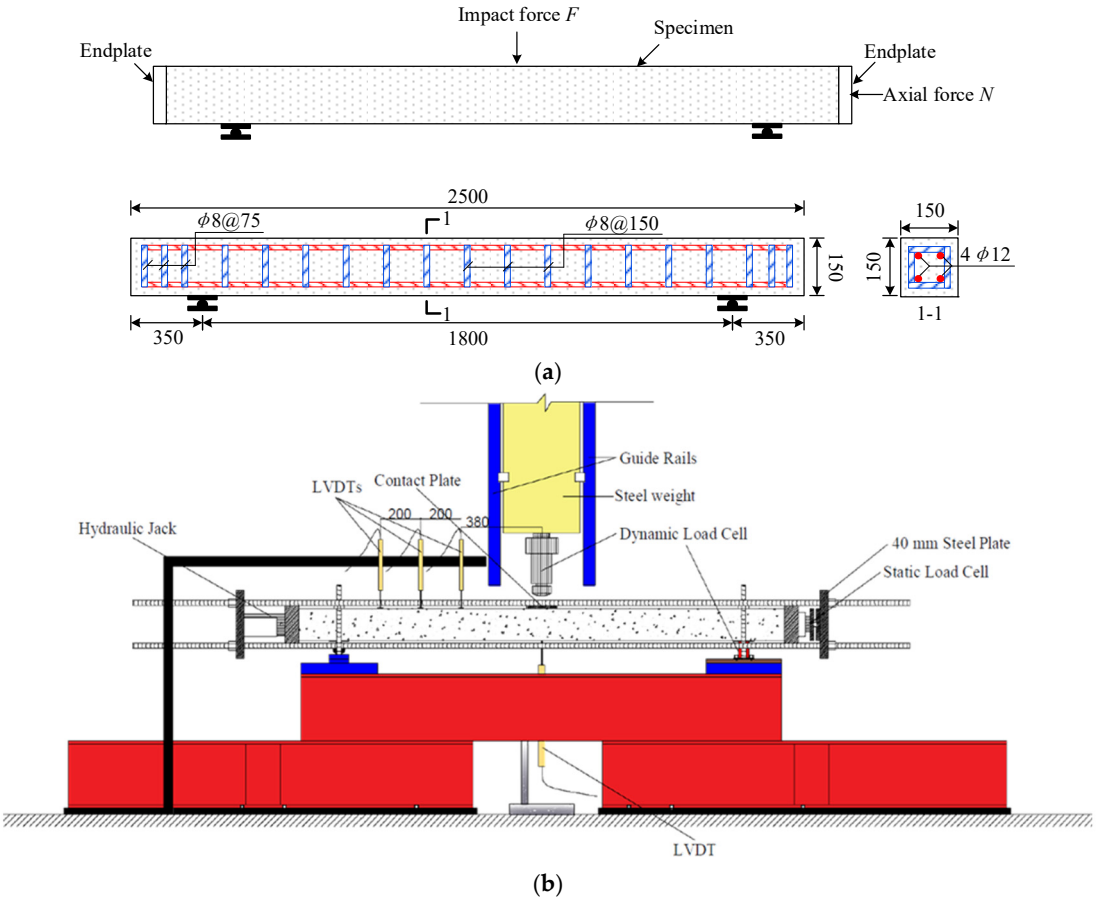



**Figure 1.** Setup of impact experiments: (**a**) simplified stress diagram; and (**b**) test setup (unit: mm).

Concrete should be treated as a heterogeneous material due to the existence of mortar, aggregates with different particle size, and randomly distributed pores. However, the established concrete FE model was usually regarded as homogeneous in previous studies. This approach ignored the influence of meso-scale heterogeneity [28]. To overcome the limitations of homogeneous models, a 3D meso-scale FE model of the experimental column was developed (Figure 2). Mortar and ITZ strengths were calibrated to 80% and 68% of the concrete strength, respectively, and preliminary tests varying ITZ thickness (4–6 mm) and aggregate volume (30–40%) showed the strength variation in less than 3%. To explore the influence of aggregate distribution on the macro-scale responses of columns, a parametric study was performed using three different random distributions of aggregates while keeping other parameters constant (denoted as Sim. distribution 1, 2, and 3 in Figure 3). The statistical results of the impact force across the three realizations are as follows: mean value = 203.33 kN, standard deviation = 14.57 kN, and coefficient of variation (standard deviation/mean) = 7.17%. The mean relative error between the simulations and the experimental result is approximately 10%. While a certain degree of variability exists due to the random aggregate arrangement, all three simulations yield impact forces within a reasonable range. Moreover, consistent with the findings in the literature [29], the influence of aggregate distribution on compressive strength, peak bearing capacity, and failure path of concrete is limited. Therefore, in this model, concrete heterogeneity was explicitly represented by random aggregate distribution (using the Monte Carlo method), a 5 mm thick interfacial transition zone (ITZ) between mortar and aggregates, and mortar representing particles smaller than 5 mm. This configuration enabled a more realistic simulation of impact-induced micro-damage. In this study, the 3D meso-scale finite element model of the experimental column was developed, as shown in Figure 2. The Monte Carlo method was adopted to generate the random distribution of aggregates. Specifically, coarse aggregates with a volume fraction of approximately 35% were assumed to be spherical and randomly distributed. The particle positions and sizes were generated iteratively under constraints to prevent overlap and ensure full containment until the target volume fraction was reached. The maximum and minimum equivalent particle size were 13 mm and 8 mm, respectively. The fine aggregates that the particle size is smaller than 5 mm and cement matrix were treated as mortar. This simplification reduced computational complexity without significantly decreasing accuracy [30].

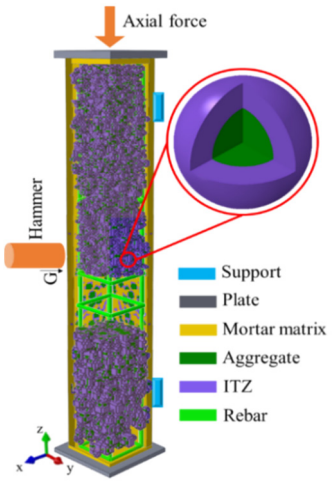



**Figure 2.** 3D simulation model of RC columns.

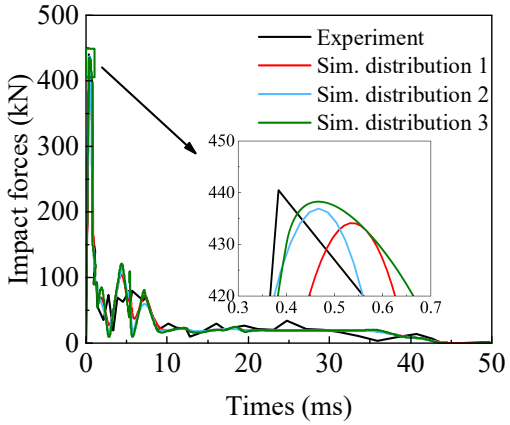



**Figure 3.** Simulation analysis of aggregate distribution.

The eight-node hexahedral reduced element and beam element were used to simulate the concrete and steel bars, respectively. The mesh size was 5 mm. Interfacial transition zones (ITZs) between the mortar and the aggregates were modeled as an equivalent material representing a mixture of the actual ITZ and part of the mortar, with a thickness of 5 mm, which enabled accurate simulation of crack propagation and damage evolution under impact. Steel bars were embedded into the concrete using the constraint "Embedded region". The reference point was established on each end of the model. The degree of freedom at the right end of the column was fully restricted, while the left end of the column was only allowed to move axially and rotate around the loading direction.

### *2.2. Constitutive Relationships*

#### 2.2.1. Constitutive Relationships of Concrete

The dynamic behavior of concrete under impact can be described using various material models, such as the Holmquist–Johnson–Cook model [31], the Karagozian and Case model [32], and the Continuous Surface Cap model [33]. However, these models were not generally used in ABAQUS/Standard 2016 due to the not well-represented tensile behavior of concrete or too many undetermined parameters [33]. Comparatively, the plastic damage model, initially proposed by Lubliner et al. [34] and further improved by Lee and Fenvens [35], was widely used in the study of the mechanical behavior of RC structures. This model describes the plastic deformation of concrete under loads and captures the stiffness degradation and strain softening phenomena resulting from the accumulation of damage in concrete. The stress–strain curve of the plastic damage model under loading is shown in Figure 4. This model assumes that the failure mode of concrete is mainly tensile cracking and compressive failure. It adopts isotropic damage variables to describe the stiffness degradation caused by tensile cracking and compressive failure. This model was used to describe the mechanical behavior of both the mortar and ITZ because of their similar microstructure compared with concrete [36]. The strength and Young's modulus of the mortar and ITZ were obtained from the literature [37], and the Poisson's ratio was determined as 0.2 [38]. Constitutive parameters of aggregate referred to Zhou et al.'s study [38], as shown in Table 1. The stress–strain relationships of concrete are presented in Appendix A, Equation (A1).

Under tensile and compressive loading, the damage in concrete is characterized by two uniaxial damage variables, $d$c and $d$t. These can be calculated as shown in Appendix A, Equations (A2) and (A3), according to the code GB 50010-2010 [39].

Thus, the stress–strain relationship formulas of the compressive ($\sigma_c$) and tensile ($\sigma_t$) stress under a uniaxial state can be obtained when $E0$ is regarded as the initial elastic stiffness, as shown in Appendix A, Equations (A4) and (A5).

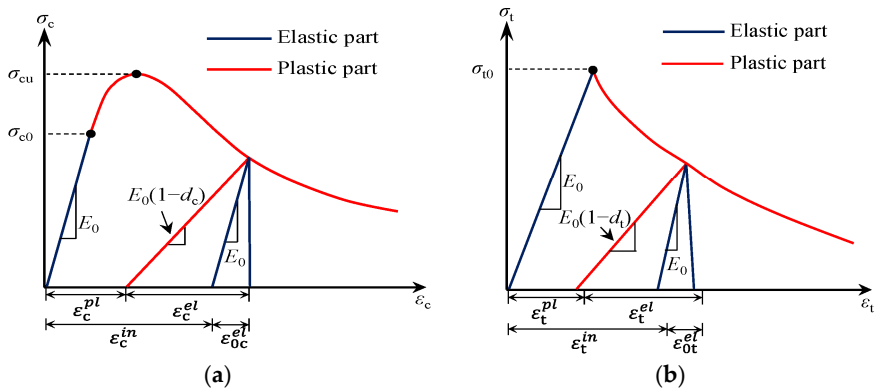



**Figure 4.** Damage plastic model of concrete: (**a**) stress–strain curve subjected to compression; and (**b**) stress–strain curve subjected to tension.

**Table 1.** Mechanical parameters of concrete meso-components at room temperature.

| Material Parameters | Aggregate [20] | Mortar [37,38] | ITZ [37,38] |
|---|---|---|---|
| Compressive strength $f_c$ (MPa) | / | 36.0 | 30.0 |
| Tensile strength $f_t$ (MPa) | / | 3.5 | 2.9 |
| Elastic modulus $E_c$ (GPa) | 70.0 | 33.0 | 30.0 |
| Poisson's ratio $\nu$ | 0.2 | 0.2 | 0.2 |
| Mass density $\rho$ [kg/m$^3$] | 2750 | 2400 | 2200 |

Hao et al. [40] found that concrete and steel are strain-rate-sensitive materials. The strain rate effect of concrete primarily manifests as an increase in material strength and elastic modulus with increasing strain rate. This study considers the dynamic increase factors of the compressive strength (CDIF), tensile strength (TDIF), and elastic modulus (MDIF) of concrete under different strain rates [41], as shown in Appendix A, Equations (A6)–(A8), where $f$cm referred to the compressive strength of concrete, as shown in Figure 5.

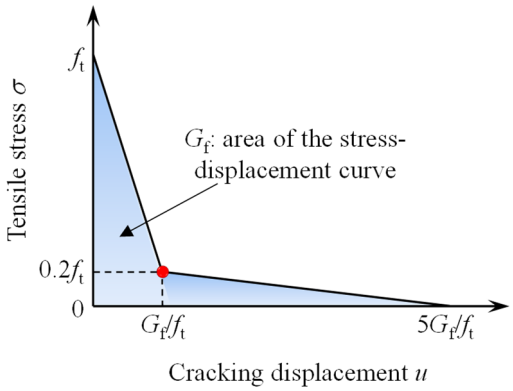



**Figure 5.** Stress-displacement curve after failure for the tensile behavior of concrete.

### 2.2.2. Constitutive Relationships of Steel

The mechanical behavior of steel rebars can be described using a simplified bilinear constitutive model because they are homogeneous materials [42]. The slope of the second line is 0.01 times that of the first line, as shown in Figure 6. Additionally, due to their sensitivity to the strain rate [40], Li et al. [43] concluded through the experiments that the elastic modulus of steel bars does not change significantly with changes in strain rate. However, their yield strength and tensile strength increase with the increasing strain rate.

A relatively weak relationship was found between the strain sensitivity of steel bars and their diameter. In order to accurately describe the effect of strain rate on the dynamic properties of steel bars, the formula recommended by CEB [44] was used. The formula reflects the impact of strain rate on the yield strength and tensile strength of steel bars. The dynamic increasing factors for yield strength (YDIF) and tensile strength (UDIF) are shown in Appendix A, Equations (A9) and (A10).

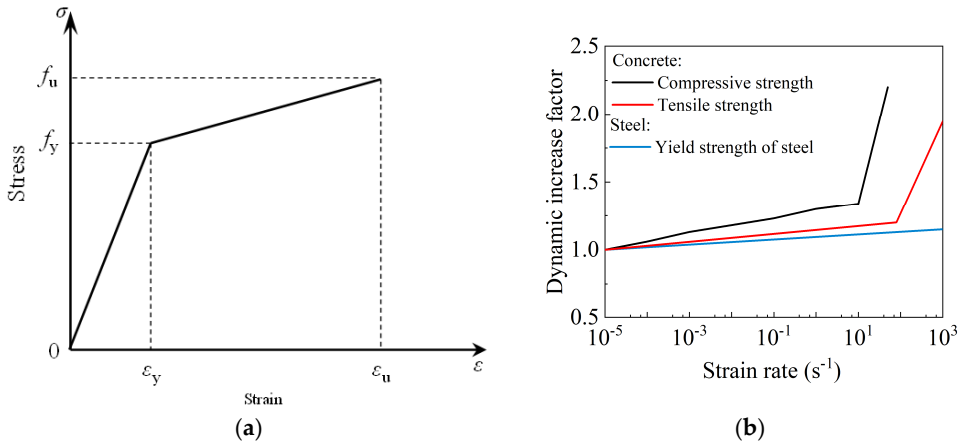



**Figure 6.** Elastic–plastic model of steel rebars and dynamic increase factor for concrete and steel: (**a**) elastic–plastic model of steel rebars; and (**b**) dynamic increase factor for concrete and steel.

### *2.3. Bond-Slip Relationships*

When RC columns are subjected to axial loads, there is a relative slip between longitudinal steel bars and concrete. The slip affects the bond performance between them. The slip between concrete and steel bars can be considered by introducing the bond-slip constitutive relationship model recommended in GB 50010-2010 [39] in the FE, as presented in Figure 7a. The characteristic points of the bond-slip relationship curve are described in Table 2. This model involves the use of a nonlinear spring element that represents the bond behavior between concrete and steel bars in the FE, as shown in Figure 7b.

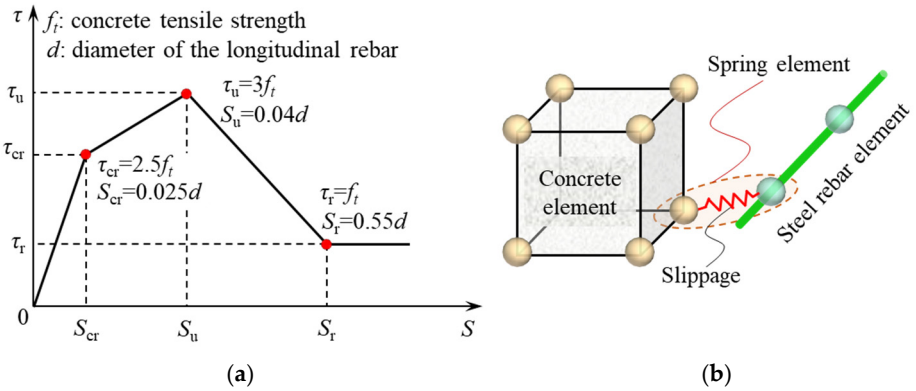



**Figure 7.** Evolution of bond-slip strength for concrete and steel with strain rate: (**a**) bond-slip relationship curve; and (**b**) spring element in the FE.

**Table 2.** Bond-slip relationship model [43].

| Control Points | Splitting Points (*cr*) | Peak Point (*u*) | Residual Point (*r*) |
|---|---|---|---|
| Bond stress (N/mm$^2$) | $2.5f_{t,r}$ | $3f_{t,r}$ | $f_{t,r}$ |
| Slip (mm) | $0.025d$ | $0.04d$ | $0.55d$ |

Figure 8 shows the sensitivity analysis results of CFRP–concrete bond behavior. Simulations 1, 2, and 3 represent bond coefficients of 1.0, 0.7, and 0.5, corresponding to perfect, reduced, and further reduced bond conditions, respectively. The test data in Figure 8 were obtained from the literature [26]. The variation in bond coefficients is realized by modifying the restraint stiffness of CFRP. The perfect-bond assumption (Simulation 1) yields the closest agreement with the experimental data, with a maximum error of less than 7% for the entire curve. When the bond coefficient is reduced to 0.7 or 0.5, the predicted load-carrying capacity decreases significantly, and the deviation from the experimental curve becomes substantial. Meanwhile, the comparison results between test and FE data under impact conditions are found to have high consistency, as shown in Figure 9. This indicates that the perfect-bond assumption is suitable for describing the CFRP–concrete bond behavior in this study, as strict surface treatment and high-quality bonding processes ensured that the actual interface did not undergo significant debonding or sliding.

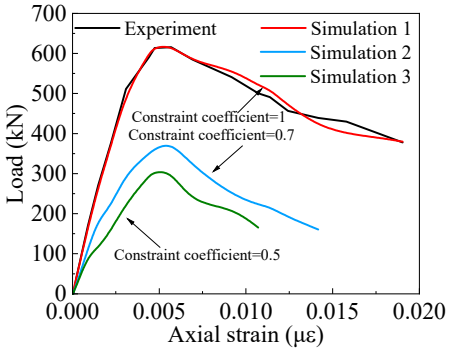



**Figure 8.** Sensitivity analysis of bond behavior between CFRP and concrete (Moshiri et al., 2015 [26]).

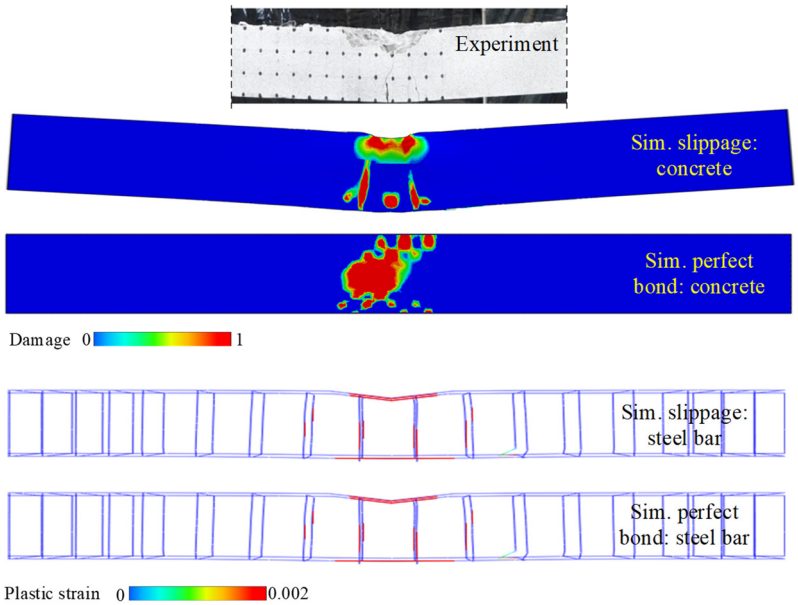



**Figure 9.** Failure patterns obtained from tests and simulations at room temperature.

## 3. Impact Behavior of RC Columns

### *3.1. Verification of Finite Element Model*

Figure 9 presents failure patterns obtained from tests and simulations at room temperature. It was observed that the failure pattern of the column considering the bond-slip relationship in the FE was same as that in the test, indicating the importance of the bond-slip relationship in the FE analysis. The bottom of steel rebars showed negligible deforma-

tion, while concrete showed significant deformation. The reason is that Figure 9 shows the deformation of the column at the time of the peak value of impact loads, when steel rebars had hysteretic deformation relative to concrete. The FE model was validated using a dual-source verification strategy based on independent experimental datasets, including impact-damaged CFRP-strengthened RC columns and one impact-damaged RC column without CFRP strengthening reported in refs. [23–26]. This approach eliminates the limitations associated with relying on a single experiment. It also confirms the model's reliability for analyzing damage mechanism. In the test, the failure of RC columns occurred at the impact location, with more severe damage at the upper part of the impact zone and only several concrete cracks at the bottom. However, no obvious cracks were observed in other areas. In the FE simulation, different colors represent the varying degrees of damage in the model. Figure 9 shows that the most severe concrete damage occurred at the mid-span due to weaker bending stiffness, and the steel bars at this location obviously bent. Three main cracks were observed at the bottom of this location due to larger tensile force, which were similar to the number of concrete cracks observed in the experiment. The comparison shows that the damage location, crack distribution, and crack number of the FE model matched the experimental results, indicating that the established FE model can accurately simulate the failure of RC columns.

Figure 10 compares the results of physical tests and simulations at room temperature. The test data in Figure 10a–d are from ref. [23]; those in Figure 10e,f are from ref. [24] (specimens BP-11, C-BP-11) and ref. [25] (specimens SCI-9, WCI-135), respectively. FE results considering the slippage of steel rebars were close to experimental results compared with those without considering slippage. This is because slippage strongly affects the cooperative interaction between concrete and steel bars. Thus, the FE results considering the slippage were used to verify the test. As shown in Figure 10a,b, the impact or reaction force evolution of the FE model was similar to that of RC columns in the experiment. The agreement is especially good within the first 10 ms. Figure 10c shows that the mid-span deflection evolution agreed well between the FE and the experiment. The deflection at 400 mm off mid-span showed a small error compared with the experiment. The reason is that the bond-slip behavior between concrete and steel bars is complex and not perfectly simulated, although the error remains reasonable. Figure 10d shows the compressive strain curve at the top of concrete obtained from the FE. It fits well with the experiment curve, revealing good accuracy for the FE model. As shown in Figure 10e,f, the impact force evolution of the FE model was similar to that of the impact-damaged RC columns strengthened with CFRP in the experiment. Overall, numerical predictions deviate less than 5% from experiments, verifying the accuracy of the model.

### *3.2. Deflection and Acceleration of RC Columns After Impact*

The impact tests for RC columns at room temperature were conducted in the literature [26], and some test results that could reflect the impact behavior of RC columns were obtained, such as impact/reaction force-time curves and deflection-time curves. However, the measured data range was not comprehensive, and some data were not obtained due to the defects of the tests. Thus, it was necessary to obtain more data to further analyze the impact behavior of columns.

Figure 11 shows the mid-span deflection at different impact times, and Figure 11 shows the acceleration of the specimen at different impact times. The maximum deflection of the column was located at the mid-span (i.e., the impact location), and it monotonically decreased with increasing distance from the mid-span, indicating the occurrence of flexural failure of RC columns subjected to impact loads. The deflection at the mid-span of RC columns exhibits a large difference when the impact time increases from 1.5 ms to 20 ms,

while the deflection only slightly increases with the increase from 20 ms to 30 ms in the impact time due to impact energy gradually consumed by the bending stiffness of the RC column. However, the deflection values of the column at different impact times show a relatively small difference when the distance from the mid-span exceeds 600 mm, as these locations are close to the supports at both ends.

Figure 12 shows that downward acceleration of the specimen gradually weakens with the increasing impact time, while the area generating acceleration expands. When impact time exceeds 5 ms, maximum acceleration at the bottom decreases 3.17%, 15.30%, and 34.84%, respectively.

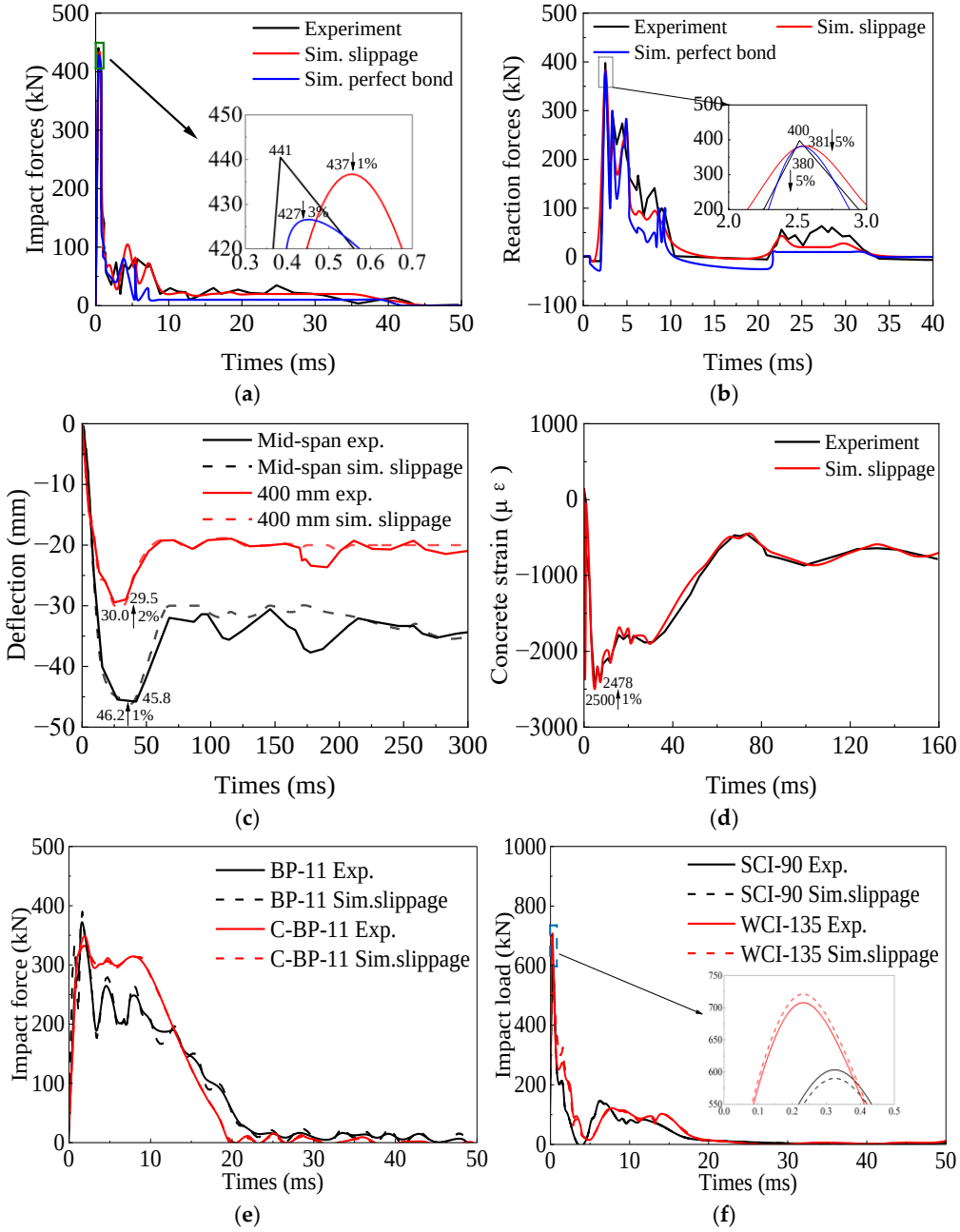



**Figure 10.** Comparison between physical test and simulation at room temperature: (**a**) time history for impact force; (**b**) time history for reaction force; (**c**) mid-span deflection and (**d**) top concrete compressive strain; (**e**) time history for impact force; and (**f**) time history for impact force.

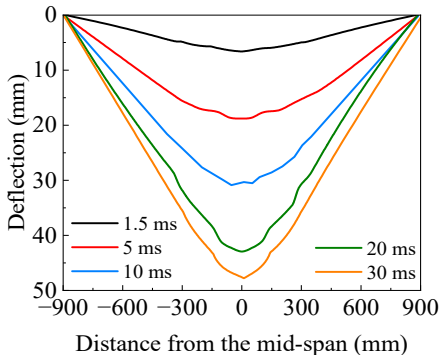



**Figure 11.** Mid-span deflection at different impact times.

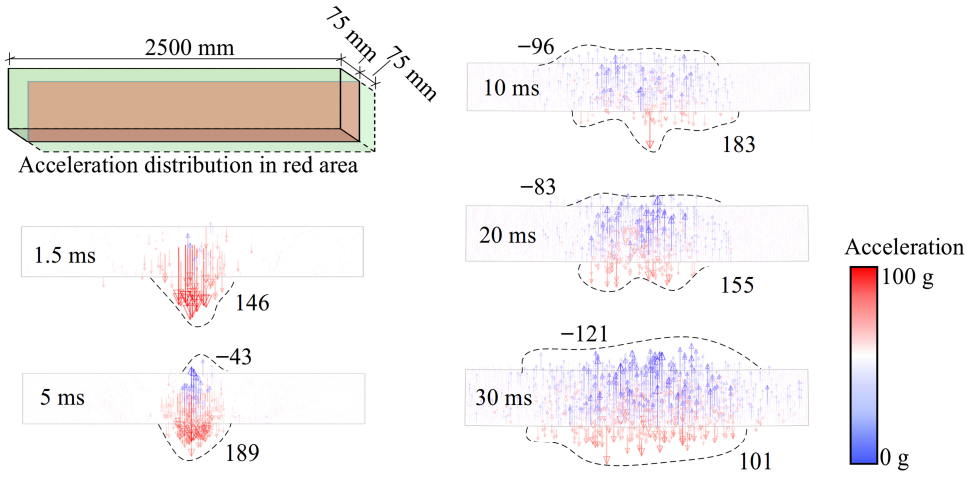



**Figure 12.** Acceleration of specimens at different impact times (unit: mm).

## 4. Strengthening of Damaged Columns

### *4.1. Strengthening Schemes and FE Model Details*

Considering that RC columns still have residual load-bearing capacity after they were subjected to impact loads, CFRP sheets can strengthen the damaged RC columns to enhance their flexural and shear performance. Figure 13 shows different types of CFRP-strengthened RC columns. A longitudinal sheet, 150 mm in width and 1800 mm in length, was bonded at the opposite side of the impact surface of the column to enhance its flexural performance, as presented in Case A. The full sheet (i.e., the longitudinal sheet was bonded on the four surfaces of the column) was bonded on the column to enhance its flexural and shear performance, with the same sheet size as Case A. To save the usage of CFRP sheets, a U-strip sheet combined with a longitudinal sheet (referred to as the U-strip sheet in the following description) was bonded on the column to enhance its impact resistance performance, with the longitudinal sheet enhancing bending resistance and short CFRP sheets, 50 mm in width and 100 mm in length, for shear resistance. In the specimen ID, the first character denotes the name of the case, and the subsequent serial numbers denote the number of CFRP layers, e.g., A-2 represents Case A, with two layers of CFRP sheets.

The S4R shell element, with a 5 mm mesh size, was employed for simulating the CFRP sheet in the FE analysis. Perfect contact between the CFRP and concrete was adopted, which was recommended by Fang et al. [45] and Wang et al. [46]. The perfect-bond assumption ignored interfacial debonding and adhesive failure, which might overestimate the strengthening efficiency and structural capacity. However, it maintains computational tractability within the already highly complex 3D dynamic meso-scale framework. The freedom degree on the left and right ends of the column was the same as that displayed

in Section 2.1. Given the anisotropic behavior of CFRP sheets, an inelastic model based on Hashin's failure criteria [47,48], involving four independent failure modes (i.e., fiber failure in tension, fiber failure in compression; matrix failure in tension, matrix failure in compression), was adopted to represent damage initiation in the FE analysis. Hashin's failure criteria were applied in this model to the CFRP layers in impact-damaged RC columns, enabling accurate simulation of dynamic fiber-matrix failure mechanisms that have rarely been considered in previous impact studies. The four failure modes are shown in Appendix A, Equations (A11)–(A14).

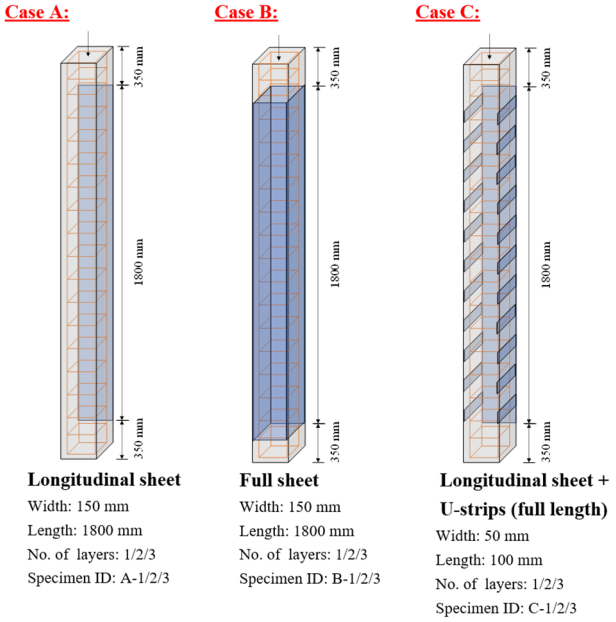



**Figure 13.** Type of CFRP-strengthened RC columns.

The damage evolution of fiber-reinforced materials in ABAQUS was assumed as the progressive degradation of material stiffness [49]. Thus, the four variables ($d_f^t$, $d_f^c$, $d_m^t$, and $d_m^c$) corresponding to the four failure modes, which were used to express the material damage, were replaced in terms of three damage parameters (fiber damage $d_f$, matrix damage $d_m$, and shear damage $d_s$), as shown in Appendix A, Equations (A15)–(A17).

To avoid mesh sensitivity during the analysis, a characteristic length was introduced into the formulation. Therefore, the equivalent displacement $\delta_{eq}$ is used for the four failure modes, expressed by the strain produced in each integration point, as shown in Appendix A, Equations (A18)–(A21).

### *4.2. Verification of FE Model Under Axial Compression*

As described in Section 2, research on the impact behavior of impact-damaged RC columns strengthened with CFRP is limited. Therefore, axial compression tests on strengthened with CFRP in the literature [26,27] were employed to verify the accuracy of the established FE model in this study. Figure 14 shows the arrangement of steel bars from ref. [26]. The column has a height of 500 mm and a cross-section dimension of 133 × 133 mm. Four longitudinal steel bars with a diameter of 12 mm were assigned in each corner of the column. The transverse reinforcement for the column comprised six stirrups with a diameter of 8 mm spaced at 85 mm. The CFRP sheet was wrapped around the column. The axial compression was applied on the column top until the failure. The experiments 2 and 3 in Figure 15 represent the specimens 1 and 2 from ref. [27], respectively.

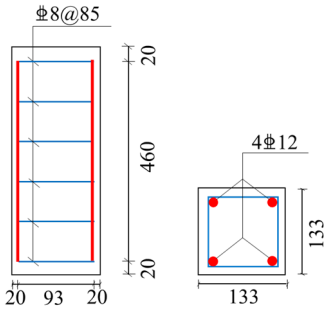



**Figure 14.** The arrangement of steel bars.

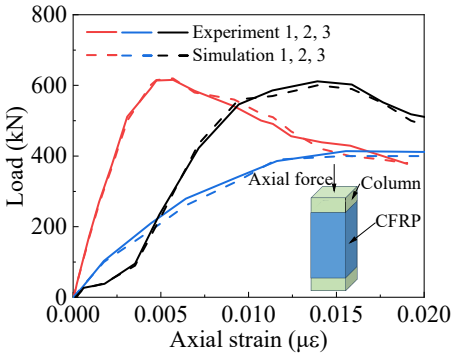



**Figure 15.** The comparison of load–axial strain curves (Moshiri et al., 2015 [26]; Ghoroubi et al., 2020 [27]).

Figure 15 compares the load–axial strain curves of different specimens. It was observed from this figure that the load–strain curve obtained from the FE model closely follows the experiment curve for all specimens, except for strains exceeding 0.015 (at which point the loading capacity decreased to 80% of the ultimate loading capacity). This indicates the FE model can reliably simulate experiment results of different cases. Peak values agree excellently with experiments, with relative errors below 1%.

## 5. Response of CFRP-Strengthened Impact-Damaged RC Columns

### *5.1. Failure Mechanism Analysis*

#### 5.1.1. Failure Patterns

Figure 16 shows the failure patterns of the columns. Specimens A-1~A-3 correspond to columns strengthened with single-sided longitudinal CFRP sheets (Case A). The CFRP sheets were bonded to the side opposite the impact prior to loading. Although the Hashin failure criterion implemented in the FE model accounts for four independent failure modes (as described in Section 4.1), the numerical results indicate that fiber tension failure dominates the CFRP sheet failure. As shown in Figure 16a,b, flexural micro-cracks were mainly concentrated in the non-impact regions. They exhibited clear through-thickness propagation, indicating limited suppression of flexural cracking. Meanwhile, the primary damage was concentrated on the impact zone. This damage manifested as localized overall failure, accompanied by longitudinal cracks extending along the free surfaces, leading to premature column failure. Therefore, although single-sided longitudinal CFRP slightly enhanced the load-bearing capacity, its effect on micro-crack development and overall ductility remained limited. Specimens B-1~B-3 correspond to columns strengthened with fully wrapped CFRP sheets (Case B). As shown in Figure 16a,b, compared with columns strengthened with single-sided longitudinal CFRP sheets, the fully wrapped CFRP columns exhibited a significant reduction in both the number and length of micro-cracks in the non-midspan impact regions. Fully wrapped CFRP effectively restrained the propagation of micro-cracks along the column length and distributed strain energy uniformly. This configuration achieved

an optimal balance between load-bearing capacity and ductility. Therefore, fully wrapped CFRP demonstrated the most significant improvement in micro-crack control, load-bearing capacity, and ductility, with three layers being the optimal configuration based on the observed failure patterns. These results agree with Liu et al. [50] and Li et al. [51], confirming that fully wrapped CFRP effectively limits shear cracks and enhances ductile behavior, reducing local damage under impact. Specimens C-1~C-3 correspond to columns strengthened with U-shaped CFRP sheets (Case C), which provide confinement to both sides and the back of the column. As shown in Figure 16a,b, flexural micro-cracks were primarily concentrated in the non-impact regions and remained non-continuous. Compared with columns strengthened with single-sided longitudinal CFRP sheets, the number and length of micro-cracks were slightly reduced. The primary damage was still concentrated near the impact zone. However, due to incomplete surface coverage, longitudinal cracks could still propagate along the free surfaces. At the same time, U-shaped CFRP effectively restrained cracks in the shear direction. Its load-bearing capacity and micro-crack control performance were intermediate between those of single-sided longitudinal and fully wrapped CFRP, effectively suppressing shear cracks in the impact region. Concrete damage decreases with more layers for fully wrapped CFRP, but changes little for U-shaped CFRP. Fully wrapped CFRP shows the most effective mesoscale coupling.

Additionally, with the increasing number of layers of the full sheet, the degree of concrete damage showed a gradually decreasing trend because more layers of CFRP could provide stronger confinement for the concrete. Specimens C-1~C-3 show the damage of RC columns strengthened by U-shaped CFRP sheets. The damage to concrete was similar to that of columns strengthened by full sheets, while the damage to the CFRP sheet exhibited a slight difference, i.e., obvious damage occurred to the short CFRP sheets on the sides of the columns, and the damage degree gradually decreased with the increasing distance from the impact position, indicating that the short CFRP sheets on the side of columns bore part of impact loads (i.e., the shear force). Additionally, the damage area and degree of concrete did not obviously change with the increase in the number of CFRP layers when the U-shaped CFRP sheet was used to strengthen the impact-damaged columns, indicating that the number of CFRP layers had a marginal influence on the strengthening effect on concrete in RC columns when U-shaped CFRP sheets were adopted. By overlaying the concrete damage contours with the CFRP fiber tension damage contours (Figure 16), a clear coupling mechanism is revealed. Severe diagonal and flexural cracks in the concrete core induce massive local expansion. This forces the wrapping CFRP to undergo extreme localized tensile strain. Once the strain exceeds the fiber tension threshold of the Hashin criterion, the CFRP ruptures locally (e.g., short strip damage on the U-wrap side). Consequently, the concrete instantly loses lateral confinement, leading to accelerated spalling. This explains why fiber tension is the primary meso-scale strengthening mechanism across all three schemes.

From the above analysis, it can be concluded that the short sheet on the side of columns for the strengthening scheme adopting U-shaped CFRP sheets effectively plays a shear resistance role. Nevertheless, the damage of RC columns strengthened with the full sheet, compared with the other two strengthening schemes, can be significantly reduced.

#### 5.1.2. Strain Distribution of CFRP Sheets

Figure 17 presents the strain distribution of the longitudinal CFRP sheet along the normalized length of columns. The maximum principal strain value of the bottom CFRP sheet (referring to the sheet at the opposite side of the impact surface of columns) was located near the mid-point of columns rather than strictly at the mid-point. Microcracks from concrete heterogeneity slightly shifted macro-scale strain peaks. The shape of the

maximum principal strain curves was similar to a normal distribution. As the normalized distance from the mid-point (impact position) increased, the maximum principal strain of the bottom CFRP sheet showed a gradually decreasing trend, with a sharper drop within the range of −0.33 to 0.33. This indicates that no matter which strengthening scheme was used, the impact load had a marginal influence on the damage of the column when the normalized distance from the impact position was larger than 0.33. As shown in Figure 16, the peak principal strain coincides with the impact-induced damage zone, while the transition region contains only minor microcracks. Fully wrapped and U-shaped CFRP sheets effectively limit the propagation of longitudinal and flexural cracks, delaying crack penetration and enhancing overall ductility.

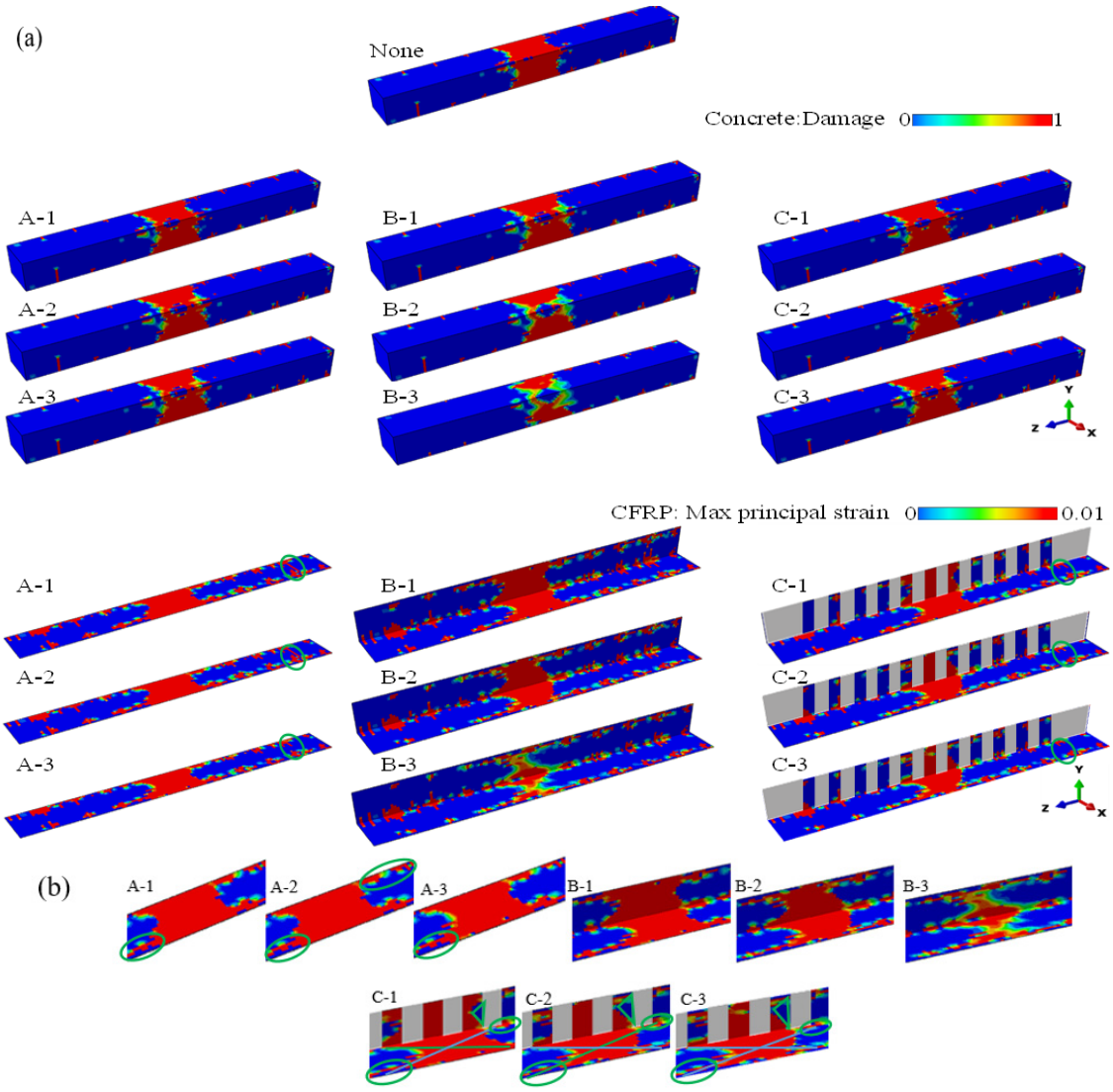



**Figure 16.** Failure patterns: (**a**) global failure; and (**b**) local failure.

It can be observed in Figure 17 that when one layer of CFRP sheets was used to strengthen the damaged columns, the maximum principal strain of the CFRP sheets in Case B and Case C was 20.7% and 19.8% smaller than that in Case A, respectively, demonstrating that the strengthening scheme in Case B and Case C, which presents a similar strengthening effect, could effectively relieve the damage of columns compared with that in Case A. This difference in macroscopic strain response originates from the distinct suppression mechanisms of internal microcracks in each scheme, as shown in Figure 16. When three layers of CFRP sheets were adopted, the maximum principal strain of the CFRP sheet in

Case B and Case C was 31.4% and 15.1% smaller than that in Case A, respectively, indicating that the damage of concrete columns could be better strengthened by wrapping three layers of CFRP sheets on the four faces of columns (i.e., the strengthening scheme in Case B). With the increasing number of CFRP layers, the peak value of the maximum principal strain for the bottom CFRP sheet in Case A decreased by 9.2% and 13.2%, by 14.5% and 20.3% in Case B, and 9.1% and 7.2% in Case C, respectively. It was found that the decline rate of the peak value of the principal strain in Case C was smaller compared with that in Case A and Case B, demonstrating that the increase in the number of U-shaped CFRP layers had a relatively smaller effect on the strengthening of damage to the column bottom. U-shaped CFRP mainly relied on bonding to confine the column bottom, and increasing layers had a limited effect on suppressing core microcracks. The peak value of the maximum principal strain in Case B presented a relatively larger decrease, especially when CFRP sheets increased from 2 layers to 3 layers, which is attributed to the reason that the full sheet had stronger confinement on the columns than the other two schemes.

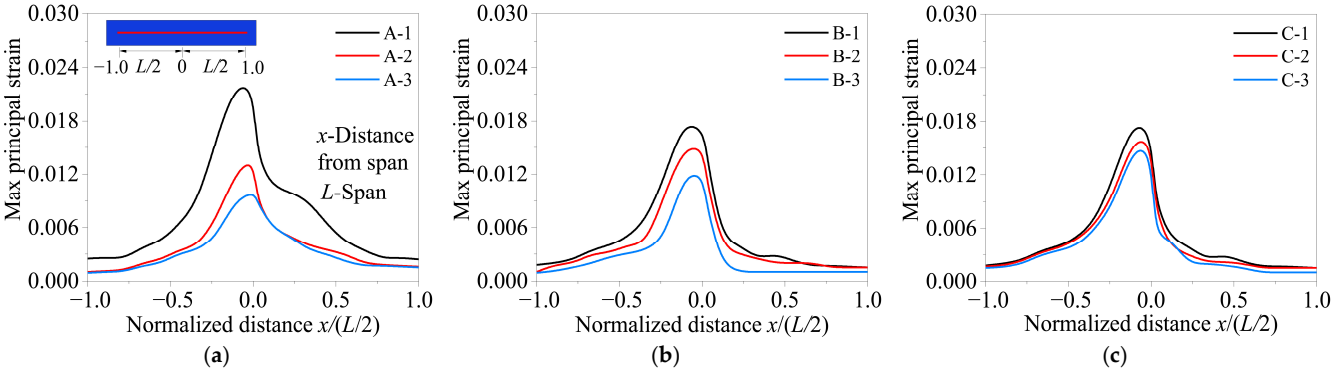



**Figure 17.** Strain distribution of bottom CFRP sheet along the normalized length of columns: (**a**) **CFRP** in Case A; (**b**) CFRP in Case B; and (**c**) CFRP in Case C.

### *5.2. Load-Axial Strain of Columns*

Figure 18 shows the normalized load–axial strain curves and the evolution of the damage element ratio (defined as the ratio of elements with PEEQ > 0.002 to total elements, indirectly reflecting the evolution of crack density) of RC columns when subjected to impact loads. It was found from the figure that the peak normalized load of columns was obviously improved with the increase in the number of CFRP layers. This indicates an effective enhancement of the actual load-bearing capacity through strengthening the impact-damaged RC columns with CFRP sheets. Compared with the unstrengthened column, the normalized strain corresponding to the peak load of the columns strengthened by CFRP sheets was larger when subjected to impact loads. This is attributed to the confinement effect of CFRP sheets on columns. Furthermore, it is clearly observed that the turning points of the damage element ratio curves are aligned with those of the load ratio curves. This indicates that the acceleration of crack propagation at the meso-scale corresponds temporally to the inflection of load-carrying capacity at the macro-scale, validating the use of the damage element ratio as an effective indicator of crack density evolution. Additionally, there is a significant difference in the damage element ratio values between unstrengthened columns and those strengthened with a single layer of CFRP. Specifically, for Cases A, B, and C, the differences reach 15.5%, 56.9%, and 27.5%, respectively. In contrast, the differences among columns with multiple CFRP layers are relatively small. This suggests that a single CFRP layer provides unstable damage suppression, whereas multiple layers offer a more consistent confinement effect.

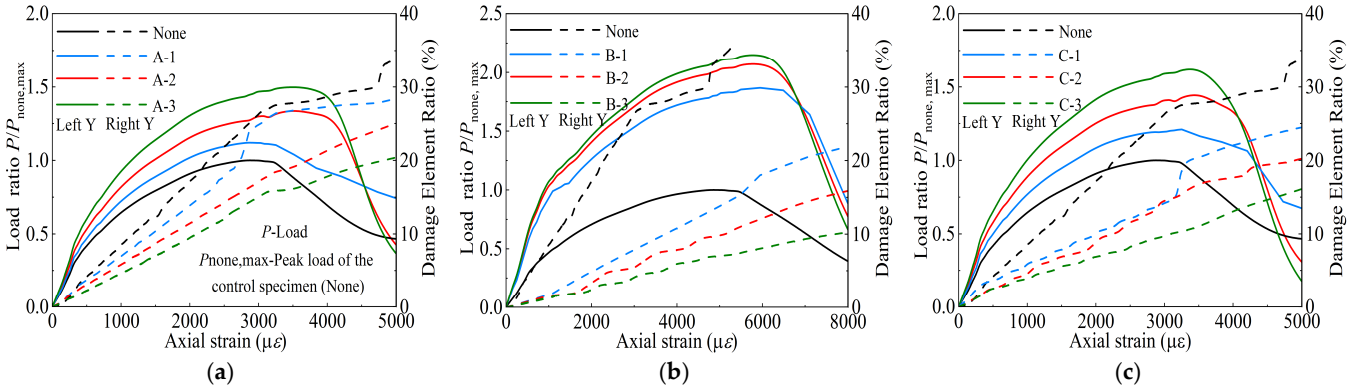



**Figure 18.** Normalized load–axial strain curves of RC columns: (**a**) Case A; (**b**) Case B; and (**c**) Case C.

When one layer of CFRP sheets was wrapped around the column, the rate of decline for the normalized curves did not obviously change compared with that for the load-strain curves of unstrengthened columns. However, when there was more than one layer of CFRP sheets wrapped around the column, the normalized load experienced a sharp decline after reaching the peak. This indicated that additional CFRP layers provided stronger confinement. However, once the CFRP cracked, concrete in the peak-load region underwent local brittle failure and rapidly failed, reflecting the evolution of the failure mode. This transition in failure mechanism is further corroborated by the damage evolution profiles. Throughout the ascending loading phase, multi-layer CFRP-confined columns exhibit a highly suppressed and stable internal damage accumulation. Ultimately, their sudden failure is governed by the abrupt tensile rupture of the CFRP sheet upon reaching its ultimate strain capacity, which stands in stark contrast to the progressive and widespread material degradation characteristic of unstrengthened columns. This agrees with Yan et al. [52], showing that multi-layer CFRP increases dynamic capacity and damage tolerance. Nevertheless, failure occurs abruptly when the CFRP jacket ruptures.

### *5.3. Mechanical Indexes*

#### 5.3.1. Loading Capacity

Figure 19 provides the load-bearing capacity of RC columns with different strengthening schemes. $P_{k0}$ denotes the load-bearing capacity of unstrengthened RC columns, while $P_k$ denotes the load-bearing capacity of RC columns strengthened by CFRP sheets. $P_k/P_{k0}$ of the unstrengthened columns was 1.0. Overall, the column strengthened by CFRP sheets had a higher loading capacity compared with that without the strengthening measure. Additionally, $P_k/P_{k0}$ of columns was found to obviously increase as the number of CFRP layers increased.

For Case A, $P_k/P_{k0}$ corresponding to specimens A-1, A-2, and A-3 were 1.12, 1.34, and 1.50, respectively. As CFRP sheets wrapped around the RC column increased from zero to three layers, $P_k/P_{k0}$ of columns experienced a growth of 12.0%, 19.6%, and 11.9%, respectively. It was found that the maximum growth rate in the load-bearing capacity of RC columns occurred when CFRP sheets increased from one layer to two layers. This might be because two layers of CFRP sheets provided the confinement that matched the bending stiffness of the column, and thus two layers of the longitudinal CFRP sheets were recommended for adoption if Case A was chosen to strengthen the impact-damaged RC columns. For Case B, $P_k/P_{k0}$ corresponding to specimens B-1, B-2, and B-3 were 1.86, 2.07, and 2.15, respectively. $P_k/P_{k0}$ of columns experienced a growth rate of 86.0%, 11.3%, and 3.8%, respectively. This indicates a gradually decreasing growth rate of the loading capacity of columns with the increase in the number of CFRP layers. This visualization provides direct insight into the previously elusive damage mechanism.

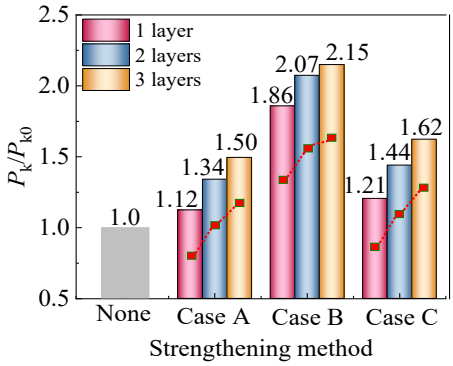



**Figure 19.** Load-bearing capacity.

The reason is due to the insufficient utilization of the confinement provided by the CFRP sheet. Thus, one layer of CFRP sheet was considered the optimal choice if Case B was chosen. For Case C, $P_k/P_{k0}$ corresponding to specimens C-1, C-2, and C-3 were 1.21, 1.44, and 1.62, respectively. The load-bearing capacity of specimens experienced growth rates of 21.0%, 19.0%, and 12.5%, respectively, indicating a larger improvement of the impact behavior of RC columns when the CFRP sheet increased from zero layers to one layer. As shown in Figure 16, U-shaped CFRP provided lateral confinement that limited shear microcracks, but the open side remained weak, allowing microcracks to develop into macrocracks. Thus, adding layers had limited benefits. From the above analysis, for Case A, the growth rate of the loading capacity of columns was larger when two layers of CFRP layers were used. However, for Case B and Case C, as the number of CFRP layers increased, the growth rate of the loading capacity of columns decreased, demonstrating that the confinement of CFRP on the column was not fully converted into the loading capacity. The reason may be due to the damage of concrete before the crack of the CFRP sheet, resulting in insufficient utilization of the confinement of the column by CFRP. This is to say that the loading capacity of columns did not match the confinement of the column by CFRP when too many layers of CFRP were used. Thus, it was recommended that a suitable number of CFRP layers be chosen.

Compared with the columns strengthened by the other two schemes, the column strengthened only by the longitudinal CFRP sheet had the smallest loading capacity due to the lack of the shear resistance. For example, when one layer of CFRP sheet was wrapped around the column, the loading capacity of columns strengthened by U-shaped CFRP sheets and full sheets was 8.0% and 66.1% larger than that of strengthened by the longitudinal CFRP sheet. This demonstrates that the shear bearing capacity of the impact-damaged column was effectively enhanced. One CFRP layer is optimal for load-bearing efficiency, as adding more layers offers diminishing returns due to premature concrete crushing, consistent with Wang et al. [46].

#### 5.3.2. Stiffness of Columns

The normalized axial compressive stiffness of RC columns is evaluated based on the tangent stiffness of the load–axial strain curve at 0.4 times the peak load. Specifically, this tangent stiffness was first calculated by taking the derivative of the load–axial strain curve at the load level of 0.4Ppeak (i.e., $\Delta P/\Delta\varepsilon$ in the vicinity of 0.4Ppeak) and then normalized by dividing it by the corresponding stiffness of the unstrengthened control column. Figure 20 presents the normalized stiffness of RC columns with and without the strengthening scheme. By comparing the stiffness of columns with the different strengthening schemes, it was found that the column strengthened by the full sheet had a larger stiffness because its bending and shear damage were well strengthened. When two or three layers of CFRP

sheets were adopted, the column strengthened by the full sheet had a close stiffness to that strengthened by the U-shaped sheet, but with a lower material usage for the U-shaped sheet. Thus, the U-shaped sheet is recommended when the stiffness of columns is heavily considered. At the early-loading stage, two to three layers of U-shaped CFRP provide sufficient confinement, making full wrapping unnecessary for enhancing axial stiffness.

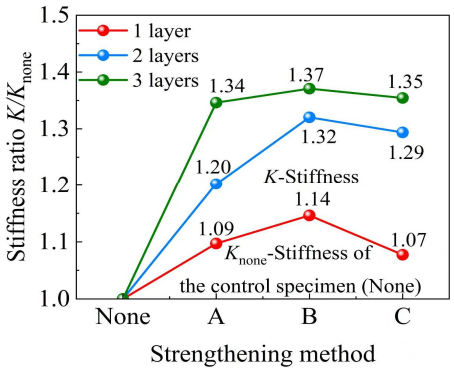



**Figure 20.** Stiffness ratio of RC columns (Case A, Case B, Case C).

For the strengthening scheme of the longitudinal sheet, the stiffness of columns increased by 9.5%, 9.6%, and 11.9% compared to the unstrengthened column when CFRP sheets increased from one to three layers. For the strengthening scheme of the full sheet, the stiffness of columns increased by 14.5%, 15.2%, and 3.8%. For the strengthening scheme of the U-shaped sheet, the stiffness of columns increased by 7.6%, 20.1%, and 4.7%. Generally, increasing the number of CFRP layers enhances the column stiffness. This is because CFRP provides lateral confinement that restricts microcrack development, delays crack propagation, and restrains bending and shear damage, as shown in Figure 16b. From the above analysis, it was found that the growth rate of stiffness of columns slightly increased with the increasing number of CFRP layers for CaseA. For Case B and Case C, the growth rate was fastest when the CFRP sheet increased from one layer to two layers. Compared with the strengthening scheme of the longitudinal sheet, the full sheet and U-shaped sheet can strengthen the shear damage of columns and provide greater confinement to prevent concrete cracking.

5.3.3. Ductility Analysis of Columns

The ductility index (DI) herein is obtained by the equation:

$$DI = \frac{\delta_{85}}{\delta_y} \quad (1)$$

where $\delta_{85}$ and $\delta_y$ denote the midspan deflection corresponding to 85% of the peak load of columns in post-peak and corresponding to the yield load, respectively. The yield point is determined using the widely accepted energy equivalence method, and the ductility index is defined as the ratio of the ultimate deflection at 85% of the peak load to the corresponding equivalent yield deflection. The ductility of all columns is compared in Figure 21. The decline in ductility with increasing CFRP layers is quantitatively attributed to confinement-induced stress concentration. This mechanism is explicitly simulated using the 3D meso-scale framework. Compared with the ductility of the unstrengthened column, columns strengthened by one layer of CFRP sheets presented larger ductility. However, an increase in the number of CFRP layers could lead to a tiny drop in ductility, irrespective of the strengthening schemes. This is attributed to the stronger confinement provided by more layers of CFRP sheets. Based on Figure 16b, the slight decrease in ductility was

attributed to the stronger confinement effect provided by additional CFRP layers. This confinement restricts the propagation of microcracks and thus reduces the overall ductility of the column.

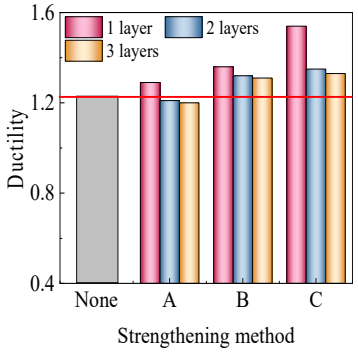



**Figure 21.** Ductility of columns.

For Case A, the ductility of the columns strengthened by 1~3 layers of CFRP sheets was 1.29, 1.21, and 1.2, respectively, and the decline rate of ductility reached 6.2% and 0.8%, respectively. For Case B, the ductility of the columns strengthened by 1~3 layers of CFRP sheets was 1.36, 1.32, and 1.31, respectively, and the decline rate of ductility reached 2.9% and 0.8%, respectively. Compared with the strengthening scheme of the longitudinal sheet, the ductility of columns was effectively improved by wrapping the full CFRP sheet. However, an increasing number of CFRP layers led to a decrease in the ductility. This is due to the stronger confinement with more CFRP layers. For Case C, the ductility of the column strengthened by 1~3 layers of CFRP sheets was 1.54, 1.35, and 1.33, respectively. The decline rate of ductility reached 12.3% and 1.5%, respectively, indicating a relatively larger decline in ductility compared with the two schemes. The increase in the number of CFRP layers resulted in an increased decline rate of ductility. When two or three layers of CFRP sheets were used, the ductility of the columns strengthened by the full CFRP sheet was close to that of the column strengthened by the U-shaped CFRP sheet. Based on comprehensive analysis, the U-shaped CFRP sheet was considered the optimal choice to improve the ductility of columns.

#### 5.3.4. Energy Dissipation of Columns

Energy dissipation, represented by the area under the load–displacement curve up to 85% of the peak load, quantifies the total structural energy absorbed, including contributions from concrete damage, steel yielding, and CFRP deformation and fracture. To facilitate comparison, the energy dissipation values are normalized into a dimensionless ratio by dividing the data of the strengthened columns by that of the unstrengthened column. Figure 22 compares the energy dissipation of RC columns strengthened with and without CFRP sheets. As illustrated in Figure 22, with the increase in the number of CFRP layers, the energy dissipation shows an increasing trend, irrespective of the strengthening scheme. Compared with the unstrengthened column (which serves as a baseline with a value of 1.0), the columns strengthened by CFRP sheets exhibit normalized energy dissipation values greater than 1.0 because CFRP sheets can absorb the energy during the deformation process of the column. When the CFRP sheet layers increase from one to three, the energy dissipation of columns for Case A improved by 12.4% and 10.4%, that for Case B by 7.3% and 1.4%, and that for Case C by 9.6% and 7.9%. It demonstrates that as the number of CFRP layers increases, the dimensionless energy dissipation of columns showed an increasing trend, which was due to the stronger confinement absorbing more energy. However, the growth rate of the normalized energy dissipation gradually decreased, because ductility

reduces with the increasing number of CFRP layers, as analyzed in Section 5.3.3. Although enhanced confinement slightly reduces the ductility of the column, its significant increase in load-carrying capacity compensates for the reduced deformation, ultimately enhancing the overall relative energy dissipation. The dimensionless energy dissipation ratio of the column increased with the number of CFRP layers, due to the CFRP restraining the propagation of microcracks, allowing the column to absorb more energy during impact. Nevertheless, the reduced ductility leads to a gradual decrease in the growth rate of the normalized energy dissipation as the number of CFRP layers increases. Compared with the three strengthening schemes, the full CFRP sheet provided the highest normalized energy dissipation for the impact-damaged column because it offers relatively stronger confinements. These results agree with Li et al. [51] and Yan et al. [52], showing that full FRP wrapping maximizes energy absorption by delaying concrete core failure and preserving structural integrity under extreme loads. Although additional CFRP layers slightly reduce ductility, the resulting significant increase in peak strength outweighs this loss. This leads to a net increase in overall normalized energy dissipation, but at a gradually declining growth rate. The primary role and effectiveness of CFRP strengthening depend on the severity of the initial damage, ranging from restoring structural integrity for slight damage to providing crucial confinement that prevents collapse for severe damage.

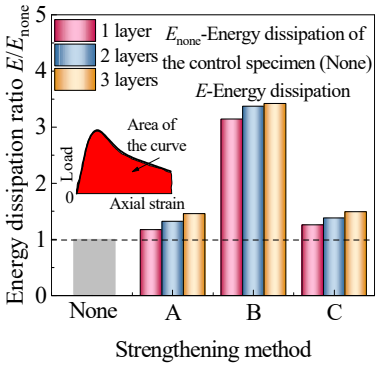



**Figure 22.** Energy dissipation ratio of columns.

## 6. Quantitative Evaluation and Design Method of Strengthening Degree

Previous studies usually focus on the damage identification method to evaluate the damage to unstrengthened columns [53], with a lack of quantitative evaluation frameworks of the strengthening degree for strengthened columns. Thus, a quantitative evaluation framework for the strengthening degree of impact-damaged RC columns strengthened with CFRP, combining the axial load-bearing capacity strengthening index and energy dissipation strengthening index, was proposed in this section. This method establishes a preliminary quantitative relationship between the strengthening level (e.g., the number of CFRP layers) and the ductility of the column.

The strengthening degree of columns can be quantitatively evaluated by strengthening indices ($D_p$ and $D_E$), which are defined as

$$D_p = \frac{P_k}{P_{k0}} - 1 \quad (2)$$

$$D_E = \frac{E_k}{E_{k0}} - 1 \quad (3)$$

where $D_p$ and $D_E$ are the axial load-bearing capacity strengthening indices and energy dissipation strengthening indices of impact-damaged RC columns strengthened with CFRP, respectively; $P_k$ and $E_k$ are the axial load-bearing capacity and energy dissipa-

tion of the columns strengthened with CFRP sheets, while $P_{k0}$ and $E_{k0}$ are those of the unstrengthened columns.

Figure 23 presents the relationship between the damage index based on energy dissipation and load-bearing capacity, where L1, L2, and L3 represent columns with 1, 2, and 3 layers of CFRP sheets, respectively. The values 0.22% and 0.35% in the bracket represent the reinforcement ratios. Because impact tests on columns with CFRP sheets under axial loads were not found, parametric FE data, including the parameters of the different layer numbers, reinforcement ratio, and column size, were used to verify the accuracy of the fitting curves in Figure 23. It was observed from the figure that the fitting curves have good accuracy. For the different layers of CFRP sheets, the strengthening degree of columns can be quantitatively evaluated according to the relationship formula between $D_P$ and $D_E$, e.g., for the three layers of CFRP sheets, the energy dissipation will increase by 29% when the axial load-bearing capacity increases by 40% due to the strengthening. It was found by the analysis of the curve slope that for the column strengthened with two layers of CFRP sheets, $D_p$ has a relatively similar growth rate to $D_E$. This indicates that the growth rate of the load-bearing capacity for the strengthened column is close to that of the energy dissipation for the column. At the time, the strengthened column shows relatively ductile failure under axial loads due to suitable constraints for two layers of CFRP sheets. However, for the column strengthened with one or three layers of CFRP sheets, a small amount of energy dissipation can result in a relatively large increase in the load-bearing capacity. At the time, the strengthened column exhibits relatively brittle failure under axial loads. This is due to insufficient constraints for one layer of CFRP sheets and excessive constraints for three layers of CFRP sheets. Thus, in the strengthening design, if the axial load-bearing capacity and energy dissipation are expected to increase in equal proportion, two layers of CFRP sheets are recommended as an optimal configuration based on the current numerical findings. If the axial load-bearing capacity is expected to increase at a higher proportion than energy dissipation, three layers of CFRP sheets are theoretically recommended. However, it should be noted that these observations are derived from a mechanistic and comparative numerical investigation. Further experimental validation and comprehensive parametric studies are required before this evaluation framework can be directly implemented in practical engineering design.

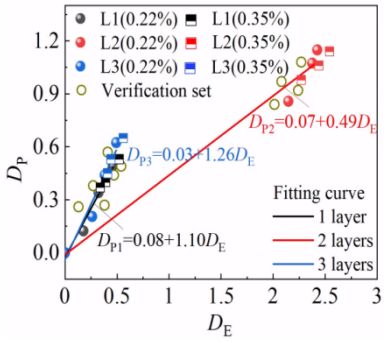



**Figure 23.** Relationship between the damage index based on energy dissipation and bearing capacity.

## 7. Conclusions

(1) CFRP sheets only bonded at one side of columns had limited influence on the crack propagation of concrete due to the smaller confinement. In contrast, U-shaped CFRP sheets could play a shear resistance role, effectively preventing inclined crack propagation. Compared with the other two strengthening schemes, the full CFRP sheet could significantly reduce the degree of damage of columns.

(2) Based on the 3D meso-scale finite element results, the loading capacity of columns significantly increased as the number of CFRP layers increased. However, the growth rate of the load-bearing capacity decreased. Compared with the other two strengthening schemes, when the full CFRP sheet increased from none to one layer, the load-bearing capacity of columns experienced a maximum growth rate, reaching 86%. This indicates the highest efficiency in enhancing load-bearing capacity and provides a clear quantitative indication of the strengthening level for impact-damaged RC columns.

(3) The stiffness of columns strengthened with U-shaped CFRP sheets was similar to that of columns strengthened with the full sheet, but with a lower material usage of U-shaped CFRP sheets than that of the full sheet. Thus, the U-shaped CFRP sheet was recommended for adoption when prioritizing the material cost.

(4) The full CFRP sheet could provide significant energy dissipation for the impact-damaged column. Additionally, for the column strengthened with full CFRP sheets, the increase in the number of CFRP layers could lead to a tiny drop in ductility and an increase in energy dissipation, regardless of the strengthening schemes. The reason for the reduction in ductility, i.e., the confinement-induced stress concentration phenomenon, could be clearly demonstrated using the 3D meso-scale model.

(5) A quantitative evaluation framework was proposed to assess the strengthening level of impact-damaged RC columns reinforced with CFRP by integrating the axial load-bearing capacity index and the energy dissipation index. The method established a preliminary quantitative relationship between the strengthening level and the ductile failure behavior of the column. The results indicated that two CFRP layers enabled the column to exhibit ductile failure under axial loading and are therefore recommended for conceptual strengthening design. The results indicate that although a single CFRP layer offers the highest efficiency in load-bearing enhancement, two layers are recommended for comprehensive strengthening to provide sufficient confinement and enable ductile failure under axial compression within the parameters of this numerical study.

Although constrained by experimental data and computational cost, the 3D meso-scale FE model developed in this study currently employs a decoupled validation strategy, a single random aggregate distribution, and a specific baseline impact scenario. Therefore, this work is primarily positioned as a mechanistic and comparative numerical investigation rather than a finalized design tool. Nevertheless, it has demonstrated sufficient accuracy and efficiency for structural-level dynamic response analysis through validation against multiple parameters such as time history for impact force, time history for reaction force, mid-span deflection, and top concrete compressive strain. Future research will further validate the 3D meso-scale model through dedicated coupled impact experiments and comprehensive parametric studies covering multiple impact energies, velocities, and boundary conditions. This will lay the foundation for more generalizable strengthening design guidelines.

**Author Contributions:** Methodology, Z.S.; formal analysis, Q.Y., Y.L. and X.L.; investigation, Y.X. and F.Z.; writing—original draft, Y.X.; writing—review and editing, F.Z., Q.Y., Y.L. and X.L.; supervision, Z.S.; funding acquisition, Z.S. All authors have read and agreed to the published version of the manuscript.

**Funding:** This research was funded by [the National Natural Science Foundation of China (Grant No.: 52478309), Shenzhen Basic Research Program (Natural Science Fund) Key Project in Basic Research (No.: JCYJ20241202123722029), China Railway Group Limited Science and Technology Research and Development Plan Project (No.: 2025-MAJOR-19), and Henan Province Science and Technology

Research Project (No.: 262102320065)]. And the APC was funded by [the National Natural Science Foundation of China].

**Data Availability Statement:** The data presented in this study are available on request from the corresponding author (the data are not publicly available due to privacy or ethical restrictions).

**Conflicts of Interest:** The authors declare no conflicts of interest. Any opinions, findings, conclusions, or recommendations expressed in this paper are those of the authors and do not necessarily reflect the views of the sponsors.

## Appendix A

$$\sigma = (1-d)D_0^{el} : \left(\varepsilon - \varepsilon^{pl}\right) \tag{A1}$$

where $d$ represents the isotropic damage variable, ranging from 0 to 1 (i.e., a larger number denotes the more severe damaged state). $D_0^{ei}$ represents the undamaged isotropic linear elastic stiffness. $\mathcal{E}^{pl}$ represents the plastic strain.

$$d_c = d_c\left(\tilde{\mathcal{E}}_c^{pl}, \theta, f_i\right) \quad 0 \le d_c \le 1 \tag{A2}$$

$$d_t = d_t\left(\tilde{\mathcal{E}}_t^{pl}, \theta, f_i\right) \quad 0 \le d_t \le 1 \tag{A3}$$

where $\tilde{\mathcal{E}}_c^{pl}$ and $\tilde{\mathcal{E}}_t^{pl}$ represent the equivalent plastic strain rates of concrete under compressive and tensile loading, respectively; $\theta$ represents the temperature; $f_i$ ($i$ = 1, 2, ...) represents other predefined field variables.

$$\sigma_c = (1-d_c)E_0\left(\varepsilon_c - \tilde{\varepsilon}_c^{pl}\right) \tag{A4}$$

$$\sigma_t = (1-d_t)E_0\left(\varepsilon_t - \tilde{\varepsilon}_t^{pl}\right) \tag{A5}$$

$$\mathrm{CDIF} = \frac{f_c}{f_{c0}} = \begin{cases} \left(\frac{\dot{\varepsilon}_c}{\dot{\varepsilon}_{c0}}\right)^{0.018} & \text{for } \dot{\varepsilon}_c \le 30\ \mathrm{s}^{-1} \\ 0.012\left(\frac{\dot{\varepsilon}_c}{\dot{\varepsilon}_{c0}}\right)^{1/3} & \text{for } \dot{\varepsilon}_c > 30\ \mathrm{s}^{-1} \end{cases} \tag{A6}$$

$$\mathrm{TDIF} = \frac{f_t}{f_{t0}} = \begin{cases} \left(\frac{\dot{\varepsilon}_t}{\dot{\varepsilon}_{t0}}\right)^{0.018} & \text{for } \dot{\varepsilon}_t \le 10\ \mathrm{s}^{-1} \\ 0.0062\left(\frac{\dot{\varepsilon}_t}{\dot{\varepsilon}_{t0}}\right)^{1/3} & \text{for } \dot{\varepsilon}_t > 10\ \mathrm{s}^{-1} \end{cases} \tag{A7}$$

$$\mathrm{MDIF} = \frac{\mathrm{E}}{E_0} = \left(\frac{\dot{\varepsilon}}{\dot{\varepsilon}_0}\right)^{0.026} \tag{A8}$$

where $f_{c0}$, $f_{t0}$, and $E_0$ represent the compressive strength, tensile strength, and elastic modulus of concrete under static loading, respectively; $f_c$, $f_t$, and $E$ represent the corresponding values at a certain strain rate; represents the strain rate, with and being $30 \times 10^{-6}\ \mathrm{s}^{-1}$ and $1 \times 10^{-6}\ \mathrm{s}^{-1}$, respectively. The fracture energy $G_f$ of the normal weight concrete was equal to $73 f_{cm}^{0.18}$.

$$\mathrm{YDIF} = \frac{f_y}{f_{y0}} = 1.0 + \left(\frac{6.0}{f_{y0}}\right)\ln\left(\frac{\dot{\varepsilon}_s}{\dot{\varepsilon}_{s0}}\right) \tag{A9}$$

$$\mathrm{YDIF} = \frac{f_u}{f_{u0}} = 1.0 + \left(\frac{7.0}{f_{u0}}\right)\ln\left(\frac{\dot{\varepsilon}_s}{\dot{\varepsilon}_{s0}}\right) \tag{A10}$$

where $f_y$ and $f_{y0}$ represent the yield strength of steel rebars at dynamic and quasi-static strain rates, respectively; $f_u$ and $f_{u0}$ represent the tensile strength of steel rebars at dynamic and quasi-static strain rates, respectively; $\dot{\mathcal{E}}_s$ and $\dot{\mathcal{E}}_{s0}$ represent the dynamic and quasi-static strain rates, respectively, in which the value of $\dot{\mathcal{E}}_{s0}$ is $5 \times 10^{-5}$ $s^{-1}$.

$$F_f^t = \left(\frac{\hat{\sigma}_{11}}{X^T}\right)^2 + \alpha\left(\frac{\hat{\tau}_{12}}{S^L}\right)^2, \hat{\sigma}_{11} \geq 0 \tag{A11}$$

$$F_f^c = \left(\frac{\hat{\sigma}_{11}}{X^C}\right)^2, \hat{\sigma}_{11} < 0 \tag{A12}$$

$$F_m^t = \left(\frac{\hat{\sigma}_{22}}{Y^T}\right)^2 + \left(\frac{\hat{\tau}_{12}}{S^L}\right)^2, \hat{\sigma}_{22} \geq 0 \tag{A13}$$

$$F_m^c = \left(\frac{\hat{\sigma}_{22}}{2S^T}\right)^2 + \left[\left(\frac{Y^C}{2S^T}\right)^2 - 1\right]\frac{\hat{\sigma}_{22}}{Y^C} + \left(\frac{\hat{\tau}_{12}}{S^L}\right)^2, \hat{\sigma}_{22} < 0 \tag{A14}$$

where $\hat{\sigma}_{11}$, $\hat{\sigma}_{22}$, and $\hat{\tau}_{12}$ represent effective stresses components; for $X^T$, $X^C$, $Y^T$, and $Y^C$, characters X and Y represent the longitudinal and transverse material strength, respectively, while superscripts T and C represent the tension and compression, respectively. $S^L$ and $S^T$ represent the longitudinal and transverse shear strength, respectively. $\alpha$ represents a contribution coefficient of the shear stress, taken as 1.0 [44].

$$d_f = \begin{cases} d_f^t & \hat{\sigma}_{11} \geq 0 \\ d_f^c & \hat{\sigma}_{11} < 0 \end{cases} \tag{A15}$$

$$d_m = \begin{cases} d_m^t & \hat{\sigma}_{22} \geq 0 \\ d_m^c & \hat{\sigma}_{22} < 0 \end{cases} \tag{A16}$$

$$d_s = 1 - \left(1 - d_f^t\right)\left(1 - d_f^c\right)\left(1 - d_m^t\right)\left(1 - d_m^c\right) \tag{A17}$$

$$\text{Fiber tension}: \ \delta_{eq}^{ft} = L^c\sqrt{\langle\varepsilon_{11}\rangle^2 + \alpha\varepsilon_{12}^2} \quad \hat{\sigma}_{11} \geq 0 \tag{A18}$$

$$\begin{gathered}\text{Fibercompression}: \\ \delta_{eq}^{fc} = L^c\langle-\varepsilon_{11}\rangle \ \ \hat{\sigma}_{11} < 0\end{gathered} \tag{A19}$$

$$\text{Matrix tension}: \ \delta_{eq}^{mt} = L^c\sqrt{\langle\varepsilon_{22}\rangle^2 + \varepsilon_{12}^2} \quad \hat{\sigma}_{22} \geq 0 \tag{A20}$$

$$\text{Matrix compression}: \ \delta_{eq}^{mc} = L^c\sqrt{\langle-\varepsilon_{22}\rangle^2 + \varepsilon_{12}^2} \ \ \hat{\sigma}_{22} < 0 \tag{A21}$$

where $L^C$ represents the characteristic length dependent on the size and type of the element. The mechanical properties of CFRP sheets, involving the anisotropic behavior, failure, and so on, were obtained from the literature [41].

## References

1. Hadi, M.N.; Jameel, M.T.; Sheikh, M.N. Behavior of circularized hollow RC columns under different loading conditions. *J. Compos. Constr.* **2017**, *21*, 04017025. [CrossRef]
2. Mai, A.D.; Sheikh, M.N.; Hadi, M.N. Investigation on the behaviour of partial wrapping in comparison with full wrapping of square RC columns under different loading conditions. *Constr. Build. Mater.* **2018**, *168*, 153–168. [CrossRef]
3. Issa, M.A.; Alrousan, R.Z.; Issa, M.A. Experimental and parametric study of circular short columns confined with CFRP composites. *J. Compos. Constr.* **2009**, *13*, 135–147. [CrossRef]
4. Hegemier, G.A.; Frieder, S.; Rodriguez-Nikl, T.; Lee, C.S.; Budek, A.M.; Dieckmann, L. *FRP-Based Blast Retrofit Design Strategies—Laboratory Tests on Rectangular RC Columns*; Report No. SSRP-2002/04; UCSD: La Jolla, CA, USA, 2002.

5. Hegemier, G.A.; Frieder, S.; Lee, C.S.; Rodriguez-Nikl, T. *FRP-Based Blast Retrofit Design Strategies—Laboratory Tests on Rectangular RC Columns—Part, II*; Report No. SSRP-2002/17; UCSD: La Jolla, CA, USA, 2003.
6. Pham, T.M.; Hadi, M.N.; Youssef, J. Optimized FRP Wrapping schemes for circular concrete columns under axial compression. *J. Compos. Constr.* **2015**, *19*, 04015015. [CrossRef]
7. Triantafyllou, G.G.; Rousakis, T.C.; Karabinis, A.I. Axially loaded reinforced concrete columns with a square section partially confined by light GFRP straps. *J. Compos. Constr.* **2015**, *19*, 04014035. [CrossRef]
8. Saljoughian, A.; Mostoffnejad, D. Axial-fiexural interaction in square RC columns confined by intermittent CFRP wraps. *Compos. Part B Eng.* **2016**, *89*, 85–95. [CrossRef]
9. Zeng, J.J.; Guo, Y.C.; Gao, W.Y.; Li, J.Z.; Xie, J.H. Behavior of partially and fully FRP-confined circularized square columns under axial compression. *Constr. Build. Mater.* **2017**, *152*, 319–332. [CrossRef]
10. Zhang, X.; Hao, H.; Shi, Y.; Cui, J.; Zhang, X. Static and dynamic material properties of CFRP/epoxy laminates. *Constr. Build. Mater.* **2016**, *114*, 638–649. [CrossRef]
11. Zhang, X.; Shi, Y.; Li, Z.X. Experimental study on the tensile behavior of unidirectional and plain weave CFRP laminates under different strain rates. *Compos. Part B Eng.* **2019**, *164*, 524–536. [CrossRef]
12. Li, Z.X.; Zhang, X.; Shi, Y. Experimental study on dynamic properties of BFRP laminates used for structural strengthening under high strain rates. *Compos. Part B Eng.* **2020**, *251*, 118731. [CrossRef]
13. Wang, W.; Zhang, X.; Chouw, N.; Li, Z.; Shi, Y. Strain rate effect on the dynamic tensile behaviour of flax fibre reinforced polymer. *Compos. Part B Eng.* **2018**, *200*, 135–143. [CrossRef]
14. Liu, X.; Li, Y. Experimental study of seismic behavior of partially corrosion-damaged reinforced concrete columns strengthened with FRP composites with large deformability. *Compos. Part B Eng.* **2018**, *191*, 1071–1081. [CrossRef]
15. Karayannis, C.G.; Sirkelis, G.M. Strengthening and rehabilitation of RC beam-column joints using carbon-FRP jacketing and epoxy resin injection. *Earthq. Eng. Struct. Dyn.* **2008**, *37*, 769–790. [CrossRef]
16. Xu, C.; Peng, S.; Liu, X.; Wang, C.; Xu, Q. Analysis of the seismic behavior of CFRP-strengthened seismic-damaged composite steel-concrete frame joints. *J. Build. Engeering* **2020**, *28*, 101057. [CrossRef]
17. Alshannag, M.J.; Alshenawy, A. Effective strengthening schemes for heat damaged reinforced concrete beams. *J. Eng. Sci.* **2020**, *32*, 236–245. [CrossRef]
18. Elghazy, M.; El Refai, A.; Ebead, U.; Nanni, A. Experimental results and modelling of corrosion-damaged concrete beams strengthened with externally-bonded composites. *Eng. Struct.* **2018**, *172*, 172–186. [CrossRef]
19. Liu, X.; Li, Y. Static bearing capacity of partially corrosion-damaged reinforced concrete structures strengthened with PET FRP composites. *Constr. Build. Mater.* **2019**, *211*, 33–43. [CrossRef]
20. Jin, L.; Lan, Y.C.; Zhang, R.B.; Du, X.L. Numerical analysis of the mechanical behavior of the impact-damaged RC beams strengthened with CFRP. *Compos. Struct.* **2021**, *274*, 114353. [CrossRef]
21. Jafari, A.; Shahmansouri, A.A.; Abdulridha, H.A.; Issa, B.I.; Bengar, H.A. Effect of CFRP confinement on bond-slip behavior of steel rebar in low-strength concrete: Experimentation, prediction and parametric study. *Constr. Build. Mater.* **2025**, *477*, 141333. [CrossRef]
22. Shahmansouri, A.A.; Jafari, A.; Bengar, H.A.; Zhou, Y. Steel rebar bond-slip behavior in CFRP-strengthened low-strength concrete: ML-driven solution and reliability analysis. *Constr. Build. Mater.* **2025**, *490*, 142302. [CrossRef]
23. Alaa, O.S.; Demitrios, M.C.; Dimitri, V.V. Effect of CFRP strengthening on response of RC columns to lateral static and impact loads. *Compos. Struct.* **2022**, *287*, 115356. [CrossRef]
24. Liu, T.; Ge, R.; Feng, F.; Chen, L.; Hao, H. Experimental study on shear behavior of square RC columns wrapped with CFRP strips under lateral static and pendulum impact loadings. *Eng. Struct.* **2025**, *335*, 120294. [CrossRef]
25. Li, R.W.; Zhang, N.; Wu, H. Effectiveness of CFRP shear-strengthening on vehicular impact resistance of double-column RC bridge pier. *Eng. Struct.* **2022**, *266*, 114604. [CrossRef]
26. Moshiri, N.; Hosseini, A.; Mostofinejad, D. Strengthening of RC columns by longitudinal CFRP sheets: Effect of strengthening technique. *Constr. Build. Mater.* **2015**, *79*, 318–325. [CrossRef]
27. Ghoroubi, R.; Mercimek, Ö.; Özdemir, A.; Anil, Ö. Experimental investigation of damaged square short RC columns with low slenderness retrofitted by CFRP strips under axial load. *Structures* **2020**, *28*, 170–180. [CrossRef]
28. Zhu, Y.; Zhang, Y.; Hussein, H.H.; Chen, G. Numerical modeling for damaged reinforced concrete slab strengthened by ultra-high performance concrete (UHPC) layer. *Eng. Struct.* **2020**, *209*, 110031. [CrossRef]
29. Jin, L. Study on Meso-Scopic Model and Analysis Method of Concrete. Doctoral Dissertation, Beijing University of Technology, Beijing, China, 2014.
30. Xiong, Q.; Wang, X.; Jivkov, A.P. A 3D multi-phase meso-scale model for modelling coupling of damage and transport properties in concrete. *Cem. Concr. Compos.* **2020**, *109*, 103545. [CrossRef]

31. Holmquist, T.J.; Johnson, G.R.; Cook, W.H. A computational constitutive model for concrete subjected to large strains, high strain rates, and high pressures. In Proceedings of the 14th International Symposium on Ballistics, Quebec, QC, Canada, 26–29 September 1993.
32. Malvar, L.J.; Crawford, J.E.; Wesevich, J.W.; Simons, D. A plasticity concrete material model for DYNA3D. *Int. J. Impact Eng.* **1997**, *19*, 847–873. [CrossRef]
33. LSTC. *LS DYNA Keyword User's Manual*; LSTC: Livermore, CA, USA, 2014; Volume 2.
34. Lubliner, J.; Oliver, J.; Oller, S.; Oñate, E. A plastic-damage model for concrete. *Int. J. Solids Struct.* **1989**, *5*, 299–326. [CrossRef]
35. Lee, J.; Fenves, G.L. Plastic-damage model for cyclic loading of concrete structures. *Mech. Eng. J.* **1998**, *124*, 892–900. [CrossRef]
36. Chen, H.B.; Xu, B.; Wang, J.; Zhou, T.M.; Nie, X.; Mo, Y.L. Parametric analysis on compressive strain rate effect of concrete using mesoscale modeling approach. *Constr. Build. Mater.* **2020**, *246*, 118375. [CrossRef]
37. Tang, L.W.; Zhou, W.; Liu, X.H.; Ma, G.; Chen, M.X. Three dimensional mesoscopic simulation of the dynamic tensile fracture of concrete. *Eng. Fract. Mech.* **2019**, *211*, 269–281. [CrossRef]
38. Zhou, W.; Zhao, C.; Liu, X.H.; Chang, X.L.; Feng, C.Q. Mesoscopic simulation of thermo-mechanical behaviors in concrete under frost action. *Constr. Build. Mater.* **2017**, *157*, 117–131. [CrossRef]
39. *GB 50010-2010*; Code for Design of Concrete Structures. Ministry of Housing and Urban-Rural Development of the People's Republic of China. China Architecture & Building Press: Beijing, China, 2010.
40. Hao, Y.F.; Hao, H. Influence of the concrete DIF model on the numerical predictions of RC wall responses to blast loadings. *Eng. Struct.* **2014**, *73*, 24–38. [CrossRef]
41. Euro-International Committee for Concrete. CEB-fip Model Code 2010. In *Fib Bulletin 55*; Euro-International Committee for Concrete: Lausanne, Switzerland, 2010.
42. Roesler, J.; Paulino, G.H.; Park, K.; Gaedicke, C. Concrete fracture prediction using bilinear softening. *Cem. Concr. Compos.* **2007**, *29*, 300–312. [CrossRef]
43. Li, M.; Li, H. Dynamic test and constitutive model for reinforcing steel. *China Civ. Eng. J.* **2010**, *43*, 70–75.
44. Comité Euro-International Du Béton. Concrete Structures under Impact and Impulsive Loading. In *CEB Bulletin No. 187*; The Committee, Ed.; Comité Euro-International Du Béton: Lausanne, Switzerland, 1988.
45. Fang, C.; Mohamed Ali, M.S.; Sheikh, A.H. Experimental and numerical investigations on concrete filled carbon FRP tube (CFRP-CFFT) columns manufactured with ultra-high-performance fibre reinforced concrete. *Compos. Struct.* **2020**, *239*, 11198. [CrossRef]
46. Wang, B.; Zhu, H.R.; Wu, X.H.; Zhang, N.Y.; Yan, B.Q. Numerical investigation on low-velocity impact response of CFRP wraps in presence of concrete substrate. *Compos. Struct.* **2020**, *231*, 111541. [CrossRef]
47. Hashin, Z.; Rotem, A. A fatigue failure criterion for fiber reinforced materials. *J. Compos. Mater.* **1973**, *7*, 448–464. [CrossRef]
48. Hashin, Z. Failure criteria for unidirectional fiber composites. *J. Appl. Mech.* **1980**, *47*, 329–334. [CrossRef]
49. Dassault Systemes Simulia Corporation. *Abaqus 6.14 User's Manual*; Dassault Systemes Simulia Corporation: Johnston, RI, USA, 2014.
50. Liu, T.; Xu, X.Q.; Chen, L.; Kim, S.; Hong, S. Numerical analysis on dynamic response of CFRP-wrapped RC columns under lateral impact loading. *Materials* **2023**, *16*, 2425. [CrossRef] [PubMed]
51. Li, R.W.; Zhang, N.; Wu, H.; Jia, P.C. Vehicular impact resistance of FRP-strengthened RC bridge pier. *J. Bridge Eng.* **2022**, *27*, 04022064. [CrossRef]
52. Yan, J.B.; Liu, Y.; Xu, Z.X.; Li, Z.; Huang, F.L. Experimental and numerical analysis of CFRP strengthened RC columns subjected to close-in blast loading. *Int. J. Impact Eng.* **2020**, *146*, 103720. [CrossRef]
53. Shi, Y.C.; Hao, H.; Li, Z.X. Numerical derivation of pressure-impulse diagrams for prediction of RC column damage to blast loads. *Int. J. Impact Eng.* **2008**, *35*, 1213–1227. [CrossRef]


**Disclaimer/Publisher's Note:** The statements, opinions and data contained in all publications are solely those of the individual author(s) and contributor(s) and not of MDPI and/or the editor(s). MDPI and/or the editor(s) disclaim responsibility for any injury to people or property resulting from any ideas, methods, instructions or products referred to in the content.